



# Turbulence and mixing by internal waves in the Celtic Sea determined from ocean glider microstructure measurements



M.R. Palmer<sup>a,\*</sup>, G.R. Stephenson<sup>b</sup>, M.E. Inall<sup>c</sup>, C. Balfour<sup>b</sup>, A. Düsterhus<sup>a</sup>, J.A.M. Green<sup>b</sup>

<sup>a</sup> National Oceanography Centre, UK

<sup>b</sup> School of Ocean Sciences, Bangor University, UK

<sup>c</sup> Scottish Association for Marine Science, UK

## ARTICLE INFO

### Article history:

Received 29 July 2014

Received in revised form 6 November 2014

Accepted 16 November 2014

Available online 28 November 2014

### Keywords:

Internal waves

Turbulence

Ocean glider

Diapycnal mixing

Autonomous systems

## ABSTRACT

We present a new series of data from a 9-day deployment of an ocean microstructure glider (OMG) in the Celtic Sea during the summer of 2012. The OMG has been specially adapted to measure shear microstructure and coincident density structure from which we derive the dissipation rate of turbulent kinetic energy ( $\varepsilon$ ) and diapycnal diffusion rates ( $K$ ). The methods employed to provide trustworthy turbulent parameters are described and data from 766 profiles of  $\varepsilon$ , temperature, salinity and density structure are presented. Surface and bottom boundary layers are intuitively controlled by wind and tidal forcing. Interior dynamics is dominated by a highly variable internal wave-field with peak vertical displacements in excess of 50 m, equivalent to over a third of the water depth. Following a relatively quiescent period internal wave energy, represented by the available potential energy (APE), increases dramatically close to the spring tide flow. Rather than follow the assumed spring-neap cycle however, APE is divided into two distinct peak periods lasting only one or two days. Pycnocline  $\varepsilon$  also increases close to the spring tide period and similar to APE, is distinguishable as two distinct energetic periods, however the timing of these periods is not consistent with APE. Pycnocline mixing associated with the observed  $\varepsilon$  is shown to be responsible for the majority of the observed reduction in bottom boundary layer density suggesting that diapycnal exchange is a key mechanism in controlling or limiting exchange between the continental shelf and the deep ocean. Results confirm pycnocline turbulence to be highly variable and difficult to predict however a log-normal distribution does suggest that natural variability could be reproduced if the mean state can be accurately simulated.

© 2014 The Authors. Published by Elsevier B.V. This is an open access article under the CC BY license (<http://creativecommons.org/licenses/by/3.0/>).

## 1. Introduction

The continental shelf breaks are critical interfaces in the Earth system. While steep topography acts to inhibit ocean–shelf exchange (Huthnance, 1995) 50% of shelf sea nutrients are estimated to arrive across the shelf break boundary (Holt et al., 2012) and disproportionately high levels of shelf sea carbon can be sequestered to the deep ocean for long-term storage (Thomas et al., 2004). The Celtic Sea shelf break is a particularly complex example due to a long series of corrugated canyon systems that connect the Celtic Sea with the Northern Atlantic Ocean. Here, the combination of strong barotropic tides and seasonal stratification acts as a high-energy internal tide generator where baroclinic energy propagates onto and away from the continental shelf. The impact of these internal waves has been shown to be dramatic at the shelf break; satellite data show a persistent band of cool surface water resulting from vertical mixing by internal

waves dissipating much of their energy close to the generation zone at the Celtic Sea shelf break that is clearly distinguishable from surrounding seasonally stratified waters (e.g. Pingree et al. (1981); Sharples et al. (2007)). Further shoreward, the effects of mixing by internal waves are less easily observed and the fate of these waves; how energy is lost, the contribution they make to mixing and their interaction with on-shelf topography is still an active area of ocean research (Nash et al., 2012).

Internal waves generated at the shelf break have been shown to propagate many wavelengths onto the Celtic shelf indicating a gradual leak of baroclinic energy over extensive distances. The rate at which this energy decays has been shown to generally agree with direct observations of the turbulent mixing rate in the pycnocline (e.g. Inall et al. (2011); Shroyer et al. (2010); Sandstrom and Oakey (1995)) suggesting that internal waves promote their own destruction via enhanced interfacial shear and wave breaking (e.g. Moum et al. (2003)). Understanding the dissipation of energy by internal waves generated at the shelf break is critically important for understanding the distribution and intensity of pycnocline mixing over continental shelf seas.

\* Corresponding author at: National Oceanography Centre, 6 Brownlow Street, Liverpool, UK. Tel.: +44 1517954800.

E-mail address: [rolm@noc.ac.uk](mailto:rolm@noc.ac.uk) (M.R. Palmer).

While the mechanisms that generate the internal wave-field are well understood (Baines, 1982) significant variability is observed in wave characteristics between sites, even between those undergoing comparable forcing. A review of internal tides over shelf seas by Nash et al. (2012) showed that while much of the character of the shelf break generated waves was predictable by harmonic analysis (Nash et al. (2012) suggests in excess of 50%) much of the remaining variability was modified by often complex stratification, dynamics and local bathymetry that is beyond the capability of regional scale models to predict. Such complexity leads to the generation of nonlinear internal waves, either directly or through modification of otherwise linear waves which become less predictable (e.g. Scotti et al. (2006)) and more prone to rapid energy loss (e.g. Inall et al. (2000)).

A recent study close to the Celtic Sea shelf break identified how short term changes in stratification modified by variable wind forcing can alter the *criticality* of wave generating conditions and on-shelf internal wave characteristics (Hopkins et al., 2014). Baroclinic energy that would otherwise be reflected into the deep ocean by a super-critical shelf slope was *released* onto the continental shelf due to reduced stratification (and subsequently sub-critical slope conditions) where it was free to propagate. Modulation of wave generating conditions by variable wind and tidal forcing at the generation zone therefore provides a candidate mechanism for producing the sporadic or *pulse-like* behaviour of the internal tide as is often observed on the continental shelf (Nash et al. (2012); Moum et al. (2008)). This mechanism may also help explain the variable propagation direction of on-shelf internal waves as different slope features (associated with the shelf break, canyons and on-shelf banks) have their potential for generation of internal waves continually altered under evolving forcing conditions.

In the Celtic Sea, where shelf break forcing is complicated by rough topography, turbulence is observed to be highly variable and patchy (Palmer et al. (2008), Palmer et al. (2013)). Long term, high-resolution measurements are therefore required to better understand turbulence and mixing attributable to internal waves and assess the spatial and temporal homogeneity of pycnocline turbulence so that an accurate picture of shelf sea mixing can be drawn.

Numerous methods have been used to measure turbulence but it is the common availability of shear microstructure probes over the last 3 decades that has led to the most rapid advance in our understanding of ocean mixing. Such probes are traditionally mounted on vertically free-falling profilers deployed from research ships, a method that brings its own limitations due to the high cost associated with sea-going research and the difficulty of undertaking repeat samples for long periods. Ship based deployments are often limited to a few hours or, as is common during shelf sea research, a few tidal cycles (e.g. Simpson et al. (1996); Palmer et al. (2013)) although extended periods covering several days have been achieved at considerable cost and effort (e.g. Moum et al. (1989); MacKinnon and Gregg (2003)). Turbulence probes have also been mounted on untethered profilers (e.g. St Laurent and Thurnherr (2007)), towed bodies (e.g. Johnston et al. (2011)) and propeller driven autonomous underwater vehicles (e.g. Boyd et al. (2010)).

While many of these methods may mitigate against some of the limitations associated with ship based deployments each method has its own caveats such as low signal-to-noise ratio (from motors or platform instability), poor control and internal power requirements. The problem of interpreting ocean turbulence measurements is exacerbated by selective sampling; the majority of measurements are understandably made in recognized mixing hotspots and avoid hazardous conditions such as extreme weather. Considering the sporadic nature of mixing and the typically short time series of turbulence measurements, we likely have a biased interpretation of shelf sea turbulence measurements to date. The ocean turbulence community would therefore benefit significantly from autonomous, reliable, cost-effective methods for collecting sustained measurements of ocean turbulence. A number of groups have been using microstructure packages attached to ocean gliders in an attempt to meet this challenge and recently published

work by Fer et al. (2014) demonstrates the capability of gliders as a suitable platform for ocean microstructure measurements.

In the following paper new results are presented from the same experiment in 2012 (FASTNET) described by Hopkins et al. (2014) and Vlasenko et al. (2014). We report on a 9-day series of observations from a specially modified ocean glider, made on the continental shelf, close to the shelf break. The glider provides coincident measurements of the vertical structure of density and the turbulent kinetic energy dissipation rate ( $\epsilon$ ). Analyses of the combined measurements are used to describe the evolution of the local internal wave-field including the turbulence and mixing associated with these waves. The paper is structured such that the experimental methods are presented in detail in Section 2. Results are presented in Section 3, summarised in Section 4 and their implications discussed in Section 5.

## 2. Methods

### 2.1. Ocean microstructure glider

Our ocean microstructure glider (OMG, Fig. 1) combines a MicroRider microstructure package (Rockland Scientific International) and a Slocum coastal electric glider (Teledyne Webb Research). The glider controls its vertical position through changes in buoyancy by decreasing or increasing its volume to dive or climb respectively. The OMG converts this vertical velocity into a horizontal see-saw trajectory using its fixed wing and dynamic pitch and ballast control. Navigation is controlled using a movable rudder. Full details of the glider operation can be found in Jones et al. (2005). The MicroRider is mounted to the upper forward section of the glider and is attached to the centre section where power is provided by the glider battery that can be switched on and off to regulate measurement periods. With this exception the MicroRider is self-contained, housing its own data collection, processing and storage. In addition to providing a platform for the MicroRider the glider also contains an integrated SeaBird CTD (conductivity, temperature and depth sensor). The MicroRider contains a suite of forward mounted microstructure probes including two shears, two temperatures and one conductivity. Only data from the shear probes will be analysed in this study, the remaining microstructure data will be the focus of a future publication. The two shear probes are orthogonally mounted; one aligned horizontally and one vertically relative to the longitudinal axis of the glider. This arrangement follows the convention of vertical profilers, designed to measure the two Cartesian components of turbulent shear. Due to the sensitivity and vulnerability of the microstructure probes, particularly during deployment and recovery, a protective guard was designed and manufactured at the UK National Oceanography Centre. The probe guard is designed to protect sensors from side impact but provide sufficient clearance of the probes throughout the operable range of glider flight path angles that physical disturbance by flow past the guard does not contaminate microstructure measurements.

It should be noted that for this mission the OMG was run using alkaline batteries that have since been upgraded to lithium cells. Future missions will have far greater endurance capability however in this study, to maximize endurance, microstructure data were generally only collected on the upward profile. Microstructure sensors did however record both upward and downward profiles during two periods (52.6 and 21.6 h) coinciding with nearby sampling with a VMP750 turbulence profiler (Rockland Scientific International; Palmer et al. (2013)). The data from the VMP750 will be used to compare with measurements from the OMG.

#### 2.1.1. Modelling the glider dynamics

Before we are able calculate meaningful turbulent parameters from the OMG we must first understand the flight dynamics of the modified glider so that its velocity, and so the flow past sensors ( $U$ ) can be calculated. Unfortunately the glider does not measure its velocity through water so we must estimate the parallel flow past the sensors

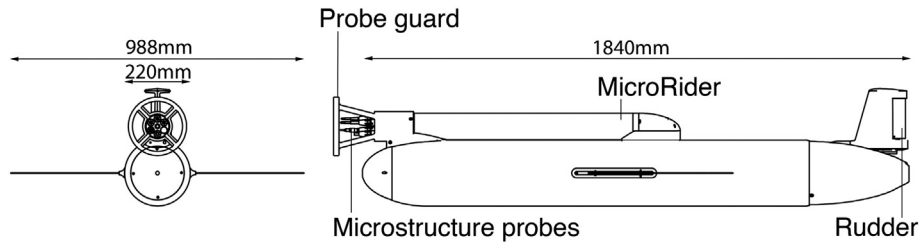


**Fig. 1.** Schematic diagram of the ocean microstructure glider, OMG. The MicroRider is shown mounted to the top of a Slocum Electric glider. The front view (left) shows the central location of the microstructure probes relative to the glider body and asymmetry of the combined OMG shape. The side view (right) shows the probe location relative to the front of the glider (tail to the right). The attached probe guard is manufactured by the UK National Oceanography Centre.

as a function of the vertical velocity derived from the change in pressure with time,  $w_p$  and the glide angle  $\gamma$ , which is the sum of the pitch angle  $\theta$  and the angle of attack  $\alpha$ ,

$$\gamma = \theta + \alpha \quad (1)$$

where  $\theta$  is derived from the fast-sampling tri-axis accelerometer housed in the MicroRider. Throughout this paper angles are considered positive above horizontal. To calculate  $\alpha$  we employ the hydrodynamic model provided by Merckelbach et al. (2010), herein referred to as MSG2010. This model has recently been successfully used to constrain estimates of  $\gamma$  and glider dynamics for a turbulence glider similar to the OMG (Fer et al., 2014). Under the assumption that over a suitably long period of time, vertical velocity estimated using the model ( $w_g$ ) should match that measured ( $w_p$ ), the model is employed to optimise estimates of  $\alpha$ . Combining and rearranging equations [13] and [14] from MSG2010 and accounting for the sign error identified in Fer et al. (2014),  $w_g$  is calculated from,

$$w_g = U \sin(\gamma) = \sqrt{-2 \sin(\gamma) \frac{(F_g - F_b)}{\rho A [C_{D0} + C_{D1} \alpha^2]} \sin(\gamma)} \quad (2)$$

where  $\rho$  is the measured in situ density and  $A$  is the surface area of the glider wings.  $C_{D0}$  and  $C_{D1}$  are coefficients representing the total parasitic and induced drag respectively, both of which are dependent on  $\alpha$  [MSG2010].  $F_g$  is the force due to gravity based on the glider mass,  $m_g = 57.56$  kg, and  $F_b$  is the net buoyancy force,

$$F_b = g\rho [V_g + \Delta V_{bp}] \quad (3)$$

where  $g$  is the acceleration due to gravity,  $V_g$  is the measured glider volume ( $56.075 \times 10^{-3}$  m<sup>3</sup>), and  $\Delta V_{bp}$  is the volume of the glider relative to neutral buoyancy at the surface which is provided by glider sensors. The effects of compressibility and thermal expansion on  $V_g$  over the 100 m depth range used in this study are negligible (MSG2010; Fer et al. (2014)) so not included. Following MSG2010  $\alpha$  is determined from,

$$\alpha = \frac{C_{D0} + (C_{D1})\alpha^2}{(a_h + a_w)\tan(\gamma)} \quad (4)$$

where  $a_h$  and  $a_w$  are lift-slope coefficients of the glider hull and wings respectively. Since Eq. [(4)] assumes that the glider is following a planar path we disregard the parts of the profile when the glider is accelerating. The mechanical volume control of the shallow-water coastal glider acts more rapidly than the oil based pumped system of the deep-water version used by Fer et al. (2014) and MSG2010. The OMG is therefore able to rapidly switch between positive and negative buoyancy with little time or distance lost due to acceleration during turning. Typical time/distance lost due to acceleration is 12 s/1.0 m during downward profiles (i.e. during both acceleration

and deceleration) and 20 s/1.6 m during upward profiles. The efficient turning capability of the Slocum coastal glider ensures almost all of the glider profile is available for use in our analysis.

With the exception of the attached MicroRider the OMG construction is near-identical to the deep-water Slocum glider used by MSG2010 so we adopt the recommended values,  $C_{D1} = 2.88$  rad<sup>-2</sup> (combining  $C_{D1,h}$  and  $C_{D1,w}$  from the original text),  $A = 0.10$  m<sup>2</sup>,  $a_h = 2.4$  rad<sup>-1</sup> and  $a_w = 3.7$  rad<sup>-1</sup>. To provide the greatest range of solutions to Eq. [(4)] the OMG was deliberately flown with a significantly different pitch angle magnitude during upward and downward profiles. Average  $\theta$  (1 std) was  $-27.53 (\pm 1.25)^\circ$  during downward profiles and  $+33.73 (\pm 1.36)^\circ$  during upward profiles. These values were close to the limits of the acceptable range within which the OMG was able to operate efficiently and, since  $\alpha$  is a function of  $\theta$  Eq. [(4)], provide the maximum possible range of values for  $\gamma$ . Solving Eq. [(4)] iteratively using a bisection technique we calculate an average  $\alpha$  (1 std) of  $-3.40 (\pm 0.16)^\circ$  and  $+2.71 (\pm 0.13)^\circ$  for downward and upward profiles respectively. Using Eq. [(4)] we generate estimates for  $w_g$  from Eq. [(2)] for a range of values for  $C_{D0}$  and minimise relative to the measured vertical velocity  $w_p$ . A best fit solution for  $C_{D0}$  is chosen as the average calculated value within a suitable time window. Due to strong tidal currents and expected energetic internal tide at our study site we use a window of two tidal ( $M_2$ ) periods rather than 24 h used by MSG2010 to ensure long term averages based on vertical velocity tend towards zero. Average (1 std) optimised  $C_{D0}$  was 0.2070 (2%) and 0.2065 ( $\hat{A} \pm 2\%$ ) for downward and upward profiles respectively. Due to the close proximity of these estimates the average value from all profiles  $C_{D0} = 0.2066$  ( $\hat{A} \pm 2\%$ ) is used for processing. The resulting average (1 std) glider speed is subsequently calculated to be 0.26 ( $\hat{A} \pm 13\%$ ) ms<sup>-1</sup> for downward profiles and 0.35 ( $\hat{A} \pm 9\%$ ) ms<sup>-1</sup> during ascent. While confidence in these values is high, represented by the low standard deviation, our estimate for  $C_{D0}$  is considerably larger than that described by MSG2010 who estimated a value  $C_{D0} \sim 0.1$  for their standard deep-water Slocum glider. Our findings indicate a near 50% increase in drag to that reported by Fer et al. (2014) for their glider with MicroRider attached ( $C_{D0} = 0.14$ ). While there may be some subtle differences between coastal and deep-water versions of the Slocum glider this increase in drag is most likely attributable to the inclusion of the MicroRider probe guard that is unique to the OMG.

### 2.1.2. Microstructure

With a reliable solution for  $U$  we may now turn our attention to the derivation of turbulent parameters. We calculate shear microstructure via the piezoceramic shear probes which regulate a voltage ( $V$ ) proportional to tangential velocity such that,

$$\frac{\partial u}{\partial x} = \frac{1}{U} \frac{\partial u}{\partial t} = \frac{V}{2\sqrt{2}GSU^2} \quad (5)$$

where  $G$  is the gain of the system amplifier and  $S$  is the calibrated sensitivity of the shear probe. Shear data are then divided into 50%

overlapping 8 s sections, equal to 4096 data points, to derive  $\varepsilon$  from the integrated shear spectrum (Wolk et al. (2002)),

$$\varepsilon_j = \frac{15}{2} \nu \overline{\left(\frac{\partial u_j}{\partial x}\right)^2} = \frac{15}{2} \nu \int_{k_1}^{k_2} \Phi(k) dk \quad (6)$$

where  $\nu$  is the kinematic viscosity of seawater. The overbar denotes a spatial average of measured shear by each shear probe ( $j$ ) along the longitudinal glider axis ( $x$ ). Integration wavenumber limits  $k_1$  and  $k_2$  are bound by glider and instrument noise, limited by the size of the sensitive region of the shear probe. Prior to analysis shear spectra are corrected for the amplifier roll-off and the limited spatial response of the shear probes is corrected for by multiplying  $\Phi(k)$  by  $(1 + (k + k_c)^2)$  after Oakey (1982) using the cutoff wavenumber of  $k_c = 48$  cpm provided by Macoun and Lueck (2004). At lower frequencies we observe significant levels of contamination that is attributed to glider motion. The lower frequency limit is therefore set to a fixed value  $k_1 = 6$  cpm, which equates to a wavelength approximately half the glider length. High frequency noise is attributable to a number of sources including eddy shedding, vibration, electronic/electrical noise and shear probe collisions with suspended sediment and biology. High frequency noise due to eddy shedding varies with energy level, however the OMG demonstrates a well defined noise level that is clearly distinguishable from the empirical model for oceanic turbulence proposed by Nasmyth (1970) (Fig. 2). The ballast pump introduces an unacceptable level of noise during measurement periods so actuation is limited to turning points only, when low glider speed and acceleration already exclude data from spectral analysis. Further motor noise is however introduced by the glider rudder that is used throughout profiling to help maintain glider heading. Thankfully rudder noise is restricted to high-frequencies outside of integration limits (Fig. 2) and has been shown to have a negligible impact on shear spectra (Fer et al., 2014). We employ a 5th

order polynomial to identify a minimum within identified noise limits of the calculated shear spectra to provide the upper integration limit  $k_2$ . Each section is checked visually to ensure spectra within the chosen limits suitably follow the predicted Nasmyth spectral shape and spikes in shear data are manually removed if they are seen to impact on power spectra within the integration limits. Unresolved regions outside of the integration limits are supplemented with predicted values provided by iteratively fitting of the energy dependent Nasmyth spectra calculated using the algorithm provided by Wolk et al. (2002).

The presence of low frequency noise due to glider motion is a major concern and forces a higher value for  $k_1$  than has been traditionally used for vertical profilers, reducing the portion of data within integration limits which is particularly acute at low energy levels (Fig. 2). Techniques have been proposed for ‘cleaning’ shear spectra using coincidentally recorded accelerometer data (Goodman et al., 2006) that are available on the OMG. This method was originally derived for microstructure measurements made from a propeller-driven AUV that is considerably faster than the OMG and less susceptible to small scale turbulent motion. The OMG is designed to be only slightly positively or negatively buoyant so is slow and more responsive to naturally occurring physical disturbance. Since turbulence is therefore likely included in glider motion, particularly at scales similar to the glider length, the methods of Goodman et al. (2006) are not valid for the OMG. As has been noted by other users (Wolk et al. (2009); Fer et al. (2014)) we observe higher energy noise in the transverse component of acceleration than the along-body or longitudinal component. This relates to a disparity in noise between the two shear probes which are orthogonally mounted. We observe not only energy to increase but also the affected wavenumber range; low-frequency motion contaminates shear even above the conservative lower integration limit ( $k_1 = 6$  cpm). The spectral spread of noise in the transverse component is likely attributable to the asymmetry of the glider shape and design, making the OMG stiffer and less susceptible to disturbance along the longitudinal axis. Without a suitable correction for this noise however we will only include data derived from the shear probe mounted horizontally (that is measuring shear in the vertical axis) in the following analysis. It is hoped that a more sophisticated solution is derived that will allow for recovery of data from vertically mounted shear probes. This is the focus of ongoing work.

The deliberate disparity between upward and downward glide angles provides a robust method for validating the calculated angle of attack and  $U$  since incorrect solutions will introduce the largest possible errors in Eqs. [(4)] and [(6)]. Assuming that over a suitable period of time, the probability density function (PDF) of  $\varepsilon$  should be the same for upward and downward profiles we can provide a rigorous test for solutions to Eq. [(4)] (Fig. 3). Comparing data from the previously mentioned 52.6 and 21.6 hour periods we find generally good agreement between upward and downward profiles of  $\varepsilon$  (Fig. 3d). There is some disparity within the low energy region ( $\varepsilon \sim 5 \times 10^{-9} \text{ W kg}^{-1}$ ) suggesting that noise levels are slightly higher during the upward profiles. Given the physical asymmetry of the OMG (Fig. 1) this is understandable. Comparing PDFs under different levels of stratification shows that during well mixed and only weakly stratified conditions ( $N^2 < 10^{-5} \text{ s}^{-2}$ ) up and down profiles are in very good agreement at all energy levels. The disparity appears to result mainly from measurements made within stratified regions. Whether this result is a consequence of the sampling angle relative to anisotropic features within strongly stratified layers is a tantalising problem to pursue and will be the focus of future work when more data are available from this and other OMG deployments. A nearby series of microstructure measurements using a VMP750 were expected to provide a direct validation of OMG results. While the general behaviour of turbulence was similar at both sites it was evident from density measurements that each was undergoing different internal forcing and so could not be directly compared. We instead

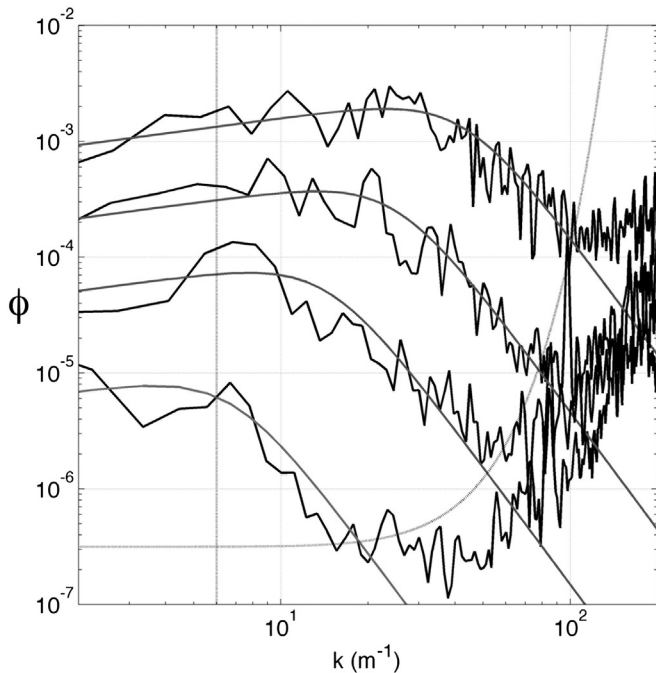


**Fig. 2.** Examples of shear microstructure power spectra (black solid), from Eq. [(5)] are shown over varying energy levels (top to bottom) of approximately  $10^{-6}$ ,  $10^{-7}$ ,  $10^{-8}$  and  $5 \times 10^{-10} \text{ W kg}^{-1}$ . Data show good agreement with equivalent Nasmyth spectra (grey solid) within the defined wavenumber limits defined by instrument length and instrument noise (vertical and curved dashed lines respectively). Spectra are shown as processed using 8-second spectra, equivalent to  $\sim 1.1/1.6$  m vertical distance for descending/ascending profiles.

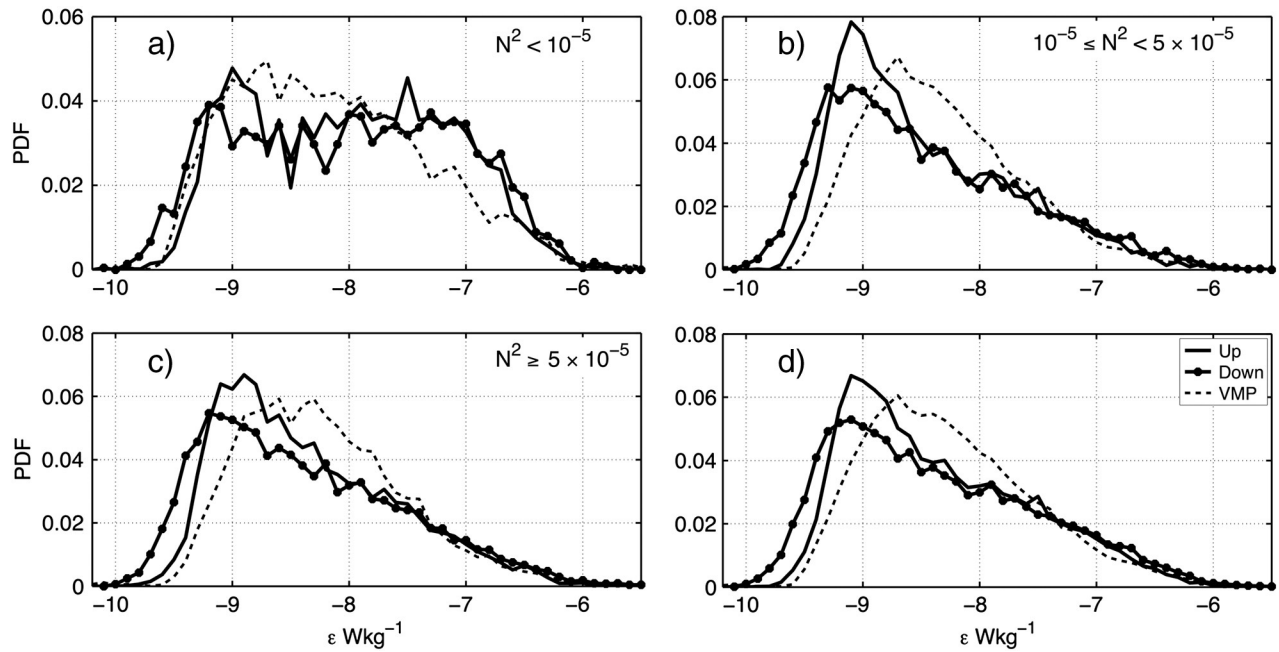


**Fig. 3.** The probability density function (PDF) of  $\varepsilon$  is shown for upward and downward OMG profiles and for nearby VMP750 profiles. Data are selected over discrete bands of stratification represented by the buoyancy frequency  $N^2 = -(g/\rho_0)(d\rho/dz)$ ; (a)  $N^2 < 10^{-5} \text{ s}^{-2}$ , (b)  $10^{-5} \text{ s}^{-2} \leq N^2 < 5 \times 10^{-5} \text{ s}^{-2}$  and (c)  $N^2 \geq 5 \times 10^{-5} \text{ s}^{-2}$ . The PDF of all comparable data are shown in (d).

compare the PDF from the two instruments which shows that the distribution of energy is similar for all profiles (Fig. 3d) and within the chosen stratification limits (Fig. 3a–c). The PDF comparison also reveals that a lower noise level is achieved with the OMG compared to the VMP750 which could explain the different distributions of energy at lower energy levels.

The 8 s, 4096 point, 50% overlapping shear spectra produce an estimate of  $\varepsilon$  for downward/upward profiles on average every 0.54/0.84 m along the glider path and 1.04/1.40 m vertically. The disparity in resolution for different glide directions being due to the shallower glider angle during dives, typically  $\gamma \sim -31^\circ$  than ascent when  $\gamma \sim -36^\circ$ .

## 2.2. Temperature, salinity and density

Conductivity, temperature and depth (CTD) were provided by standard payload sensors (Sea-bird Electronics) housed in the central section of the OMG and are used to calculate salinity and density. CTD data were collected at 1 Hz during periods when the MicroRider was operative. Errors in salinity and density may occur due to inconsistencies between temperature and conductivity sensors, which are partly attributable to the physical separation of sensors and a disparity in response times, both of which can be simply corrected for. More complex however is the correction for thermal inertia of the conductivity cell (Lueck and Picklo, 1990). Best practice recommends using a pump to provide a regular flow, high flow rate through the conductivity cell. This is not possible on the OMG as it would introduce an unacceptable level of mechanical noise to the shear microstructure data. Flow through the cell is therefore slow and irregular, forced only by the surrounding flow as the glider travels through the water and is restricted by a narrow internal radius. To calculate flow through the conductivity cell we assume a laminar flow equivalent to circular Poiseuille flow (Kundu, 1990) forced at the cell entrance by  $U$ . The magnitude and inverse relaxation time of the thermal anomaly associated with the conductivity cell may then be calculated following the methods of Lueck and Picklo (1990) by scaling parameters based on flow speed by the estimated flow through the cell. This process is non-trivial and requires a number of assumptions which highlight the challenges of making accurate salinity measurements using slow moving gliders, particularly those

with un-pumped CTDs. For a typical glider speed  $U = 0.3 \text{ ms}^{-1}$ , flow in the conductivity cell is estimated to be as little as  $0.13 \text{ ms}^{-1}$ . The cell relaxation time ( $\beta^{-1}$  in Lueck and Picklo (1990)) is around 80 s which is far higher than that of a standard ship deployed CTD which is typically 7 s. Using calculated values to account for the thermal anomaly significant improvements are achieved in salinity and are considered of sufficient quality for density to be derived directly from in situ CTD measurements.

Best practice recommends using a pumped system to increase the flow rate through the conductivity cell to minimise inconsistencies between the temperature and conductivity sensors that might lead to errors in salinity and subsequently density.

The glider provides measurements of temperature, salinity and density from the full range of the typical 10 m to 100 m depth. To investigate the changing vertical density structure over the entire water column however we need to extend the observed data to provide a realistic estimate of the density down to the sea bed and up to the surface. The elliptical nature of the relatively strong tidal currents makes it reasonable to assume that the bottom boundary layer (BBL) is well mixed over the unresolved lower portion of the water column, typically down to 140 m. It is not however possible to simply extrapolate the observed density structure since there are regular isopycnal displacements due to internal wave activity that push the pycnocline into, and sometimes beyond, the lower extent of the glider profile. BBL density is therefore not always realised on each profile. We therefore extend the glider density profile assuming that the BBL density is equal to the maximum density within a window equivalent to semidiurnal tidal period ( $M_2$ ,  $\sim 12.42 \text{ h}$ ). Where the maximum density is not realised within an individual profile the pycnocline is extended using a cubic interpolation with an assumed minimum BBL depth of 120 m, assumed from occasional nearby independent CTD measurements. A similar method is employed for extrapolation of the near surface layer. Fig. 4 demonstrates the pycnocline shape preserving the nature of the method.

To study the energetics of the internal wave-field we use the extended density data to calculate the available potential energy (APE), which is often defined as the active component of the potential energy that can be converted to kinetic energy and may contribute to turbulent mixing (Moum et al., 2007; Lamb, 2007). We calculate APE using the

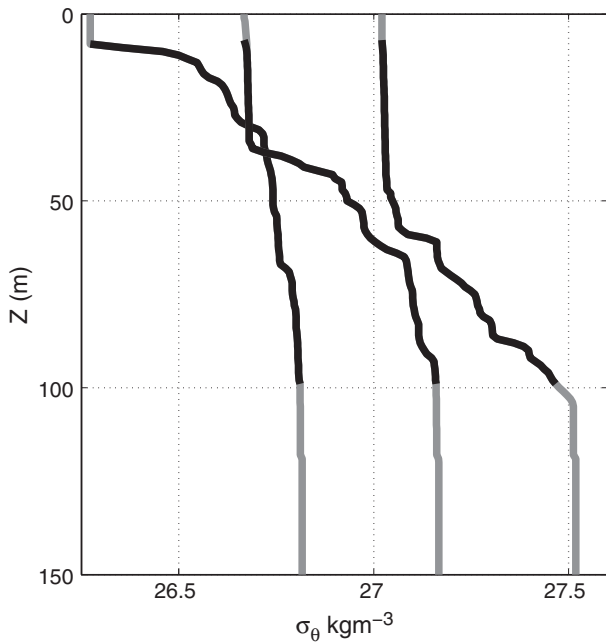


**Fig. 4.** Example density profiles showing measured (black) and extended (grey) regions. In the vast majority of cases the OMG covered the entire pycnocline region.

methods suggested by Kang and Fringer (2010) for nonlinear internal wave-fields,

$$APE = \int_{z-\zeta}^z g[\rho(z) - \rho(z')] dz' \quad (7)$$

where the square brackets contain the difference between a reference density profile,  $\rho(z)$ , and the measured density profile  $\rho(z')$  that has been displaced distance  $\zeta$  by a passing internal wave. For our analysis we calculate  $\rho(z)$  from a moving window average equivalent to the tidal ( $M_2$ ) period.

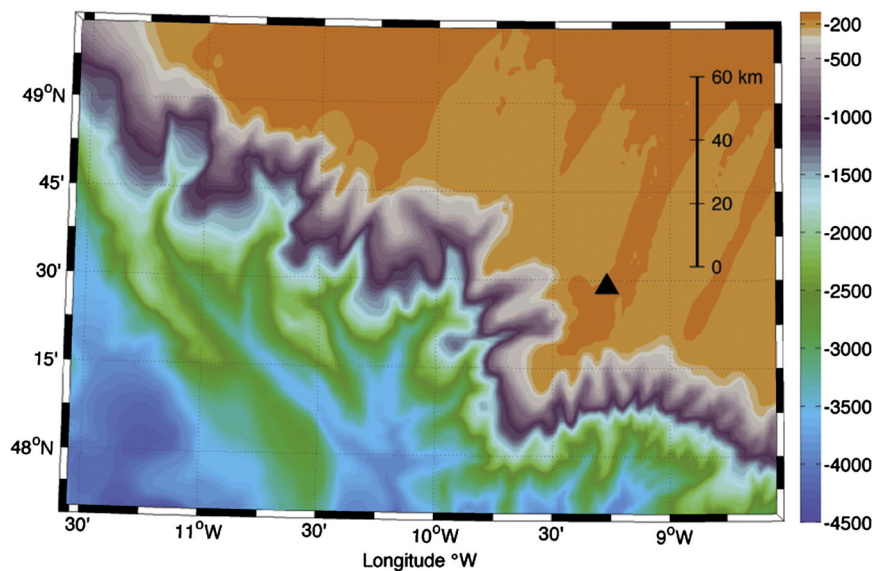
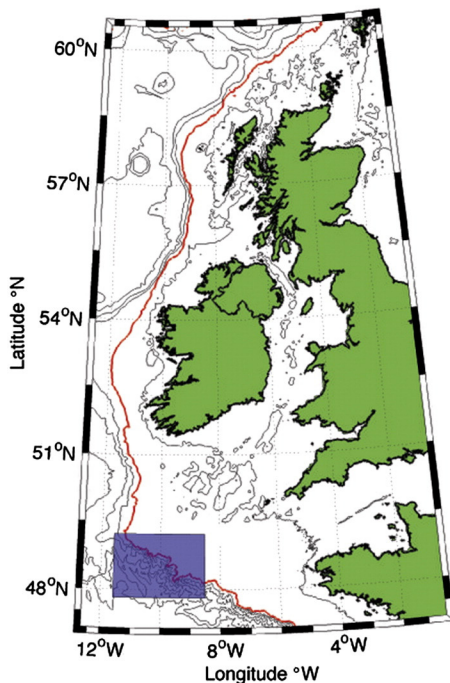


**Fig. 5.** The deployment area is shown relative to the UK and Ireland (left panel) and in more detail (right panel) with local topography (GEBCO). The central glider position, station ST3.5, is indicated by the black triangle.

### 2.3. Mission

The OMG was deployed from the RRS Discovery during its 376th research cruise as part of the FASTNet (Fluxes Across Sloping Topography of the North East Atlantic) research programme. The glider was deployed at station ST3.5 (48°28.9' N 9°16.2' W) which was 140 m deep and approximately 20 km from the Celtic Sea shelf break (Fig. 5). The OMG mission was designed to maintain a position typically within 2 km of its deployment location. The glider profiled continuously over an operable range of between 10 and 100 m depth interrupted by 2 hourly surface stops for satellite positioning and communication. Each 2-hour period typically provided 5 to 6 return (down and up) profiles. These shallow dives were designed to provide the highest temporal resolution of the seasonal thermocline while capturing the vertical excursion of a highly active internal wave field.

Due to the relatively short distance of the glider track and its slow horizontal speed we will consider the OMG data to be quasi-stationary at ST3.5. The OMG recorded data between 11:26 (UTC) 18th June to 08:33 27th June 2012. Following preliminary shallow test dives (4 h) a total of 209 profiling hours and 766 individual profiles were collected of which 673 reached full or near-full operational depth. Data collection was interrupted for approximately 7 h (18th June 23:40 to 19th June 06:17 UTC) due to a temporary technical fault relating to satellite communications.

The summer weather on the Northwest European Shelf was typically variable; a strong gale on the 15th June (day 166 in Fig. 6) delayed deployment of the glider and winds in excess of  $10 \text{ ms}^{-1}$  were observed mid-way through the deployment.

## 3. Results

### 3.1. Density structure

Density structure (Fig. 7) shows the area is strongly vertically stratified throughout the deployment period with an average (1 std) density difference between bottom and surface mixed layers of  $0.56 (\pm 0.09) \text{ kg m}^{-3}$ . Density structure is predominantly temperature (Fig. 7a) controlled (accounting for 97.14% of variance) although a fresher surface

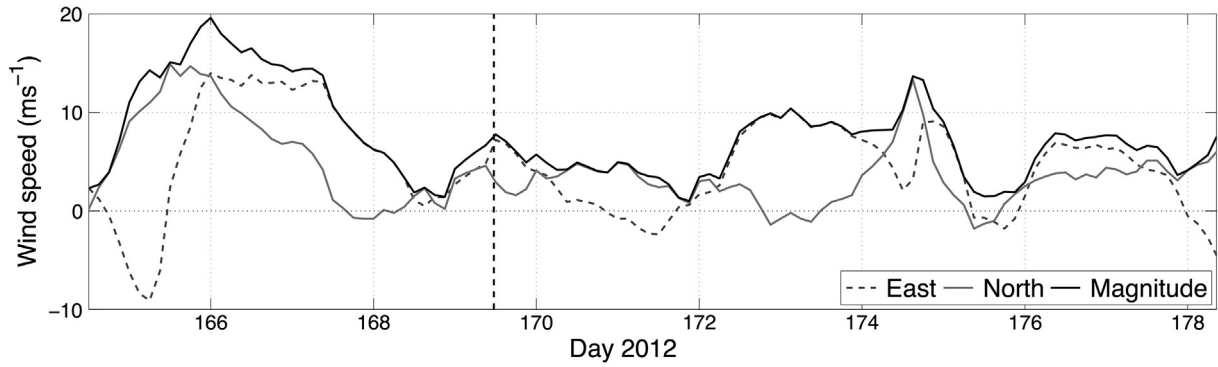


**Fig. 6.** Strong winds during the week prior to the OMG deployment (indicated by the dashed vertical line) are replaced a quiescent period up to day 172 when winds rapidly increase in easterly winds  $\sim 10 \text{ ms}^{-1}$ . A second peak is observed at day 174.7 followed by a rapid decrease in wind strength. Wind data are provided by the extended-range reanalysis (ERA) Interim product [ECM] of gridded wind fields from the European Centre for medium-range weather forecasting (ECMWF).

layer (salinity, Fig. 7b) persists that contributes positively to stable stratification. Surface temperature steadily increases up to day 174 from around  $13.5 \text{ }^\circ\text{C}$  to over  $14 \text{ }^\circ\text{C}$  before cooling slightly for 2 days and then recovering a steady increase to a maximum of  $14.8 \text{ }^\circ\text{C}$  by the end

of the 9 day period. The observed drop in surface temperature coincides with a peak in wind speed around day 174.75 (Fig. 6). Generally well mixed surface and bottom mixed layers (SML and BML) were separated by a pycnocline that ranged from 30 to 80 m thick (Fig. 7) with an

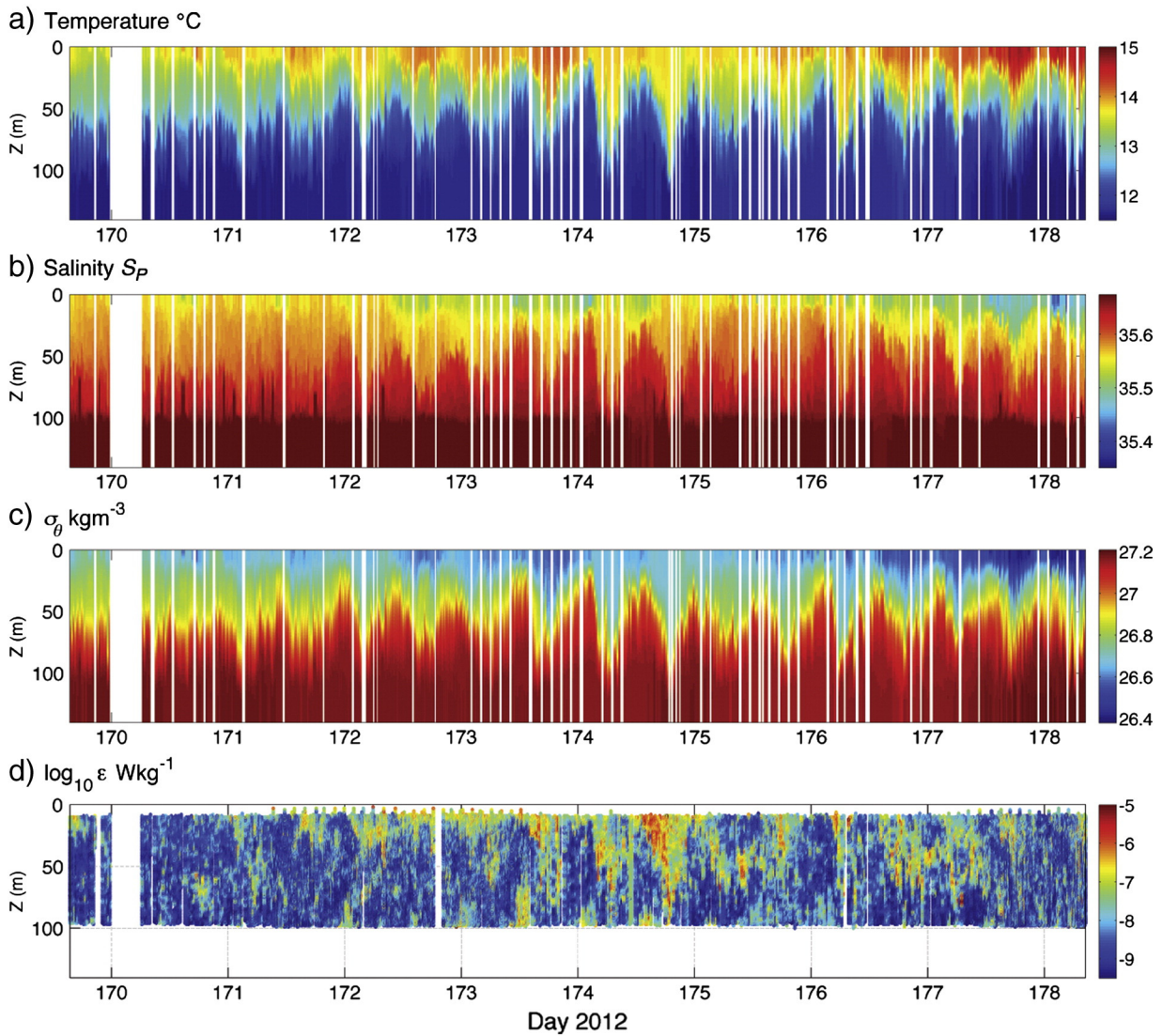


**Fig. 7.** (a) Temperature, (b) salinity, (c) potential density ( $|\rho|$ ) and (d)  $\log_{10} \hat{\mu}$  measured by the OMG. Data in the upper 3 panels have been extended to cover the entire water column. White sections in these panels indicate a four hour period of communication failure (from day 170) and sections when insufficient data was collected for using the extension method described in Section 2.2. Data from these periods was not used in the analysis.

average (1 std) of 56.1 m ( $\pm 11.8$ ). Here we define the SML and BML as the water above and below the 10th and 90th percentiles of the vertical potential density profile range respectively for any given time. The SML is generally shallow, on average (1 std) = 18.6 m ( $\pm 10.2$ ) deep although pycnocline perturbations can draw the SML down to over 50 m deep at times.

Density data reveals a highly active internal wave-field with vertical isopycnal displacements occasionally exceeding 50 m, equivalent to over one third of the total water depth. The largest displacements are attributable to low frequency internal waves observed to be close to the semi-diurnal lunar frequency ( $M_2$ ) which has been shown to be the dominant tidal frequency at the nearby shelf break (Green et al., 2008) and on-shelf (Hopkins et al., 2014). Identification of the true frequency of internal waves observed with the OMG is complicated since this would require exact knowledge of the sub-surface glider velocity and the propagation direction and velocity of the internal waves. The complexity of the Celtic Sea internal wave-field and associated baroclinic velocities, especially this close to the shelf break, makes estimation of these parameters impossible. Recent work at a nearby sites (Hopkins et al., 2014; Vlasenko et al., 2014) has however shown that the local internal wave field was dominated by the semi-diurnal internal tide propagating from the nearby shelf break so we will refer to these low mode oscillations as such. Higher frequency internal waves are also observed throughout the 9 days of deployment evident as short term fluctuations in isopycnal height.

### 3.2. Internal waves and APE

The magnitude of the internal tide varies considerably over time. While the full spring-neap cycle is not resolved within the 9 day time-series, nearby measurements (as reported in Hopkins et al. (2014)) indicate that spring tides occur on day 174. Prior to day 171.5 no internal tide is identified however high frequency displacements are evident throughout. Following this period a low frequency oscillation is observed close to the tidal frequency for the remainder of the deployment period. The internal tide is observed to increase in magnitude close to spring tides, notably between days 173.5 and 175 when three successive large waves are observed with associated

pycnocline displacements in excess of 50 m (Fig. 8). Following this high-energy period the internal tide appears to be somewhat interrupted for two tidal cycles, when pycnocline displacements are dramatically reduced, before returning to a more energetic state.

To examine the active energy attributable to the internal wave-field we here consider the depth integrated APE calculated from Eq. [(7)] (Fig. 9). Intuitively, APE closely follows the isopycnal height variability as seen in the density data (Fig. 7c); peak energy is associated with the troughs of large amplitude low-frequency internal waves occurring during the previously identified high energy period, days 173.5 to 175, and during days 176 and 177. To better examine the contribution from the internal tide we apply a moving  $M_2$  period (12.42 h) average to the APE data (Fig. 9c, black line). The internal wave-field is shown to be continuously energetic,  $AP E_{M_2}$  maintaining values above  $200 \text{ J m}^{-2}$  throughout. The dominance of the two high energy periods is now more evident; in the first of two peak energy periods associated with the spring tide a gradual increase in  $AP E_{M_2}$  is observed from day 173.15, peaking at day 174.35 before reducing gradually to a minimum at day 175.25. Later, a relatively short-lived increase in  $AP E_{M_2}$  is observed centred on day 176.25 coincident with a single high amplitude internal wave. Following this period  $AP E_{M_2}$  maintains an elevated level of energy around  $0.65 \text{ kJ m}^{-2}$  until the end of the glider deployment period.

The APE is of course only one component of the total baroclinic energy budget but it was not possible to resolve the associated kinetic energy (KE) attributable to these internal waves without local measurements of baroclinic velocity. We do however consider APE as indicative of the total energy available for mixing from the internal wave-field since wave theory tells us that the suitably averaged kinetic and potential energy densities are equal for linear internal waves and observations of non-linear internal waves, despite some considerable scatter, have also shown close agreement (e.g. Moum et al. (2007)).

### 3.3. The dissipation rate of turbulent kinetic energy, $\epsilon$

The OMG provides measurements of  $\epsilon$  between 10 m and 100 m depth and so provides coverage of the majority of the active pycnocline region during the deployment. Background levels of  $\epsilon$

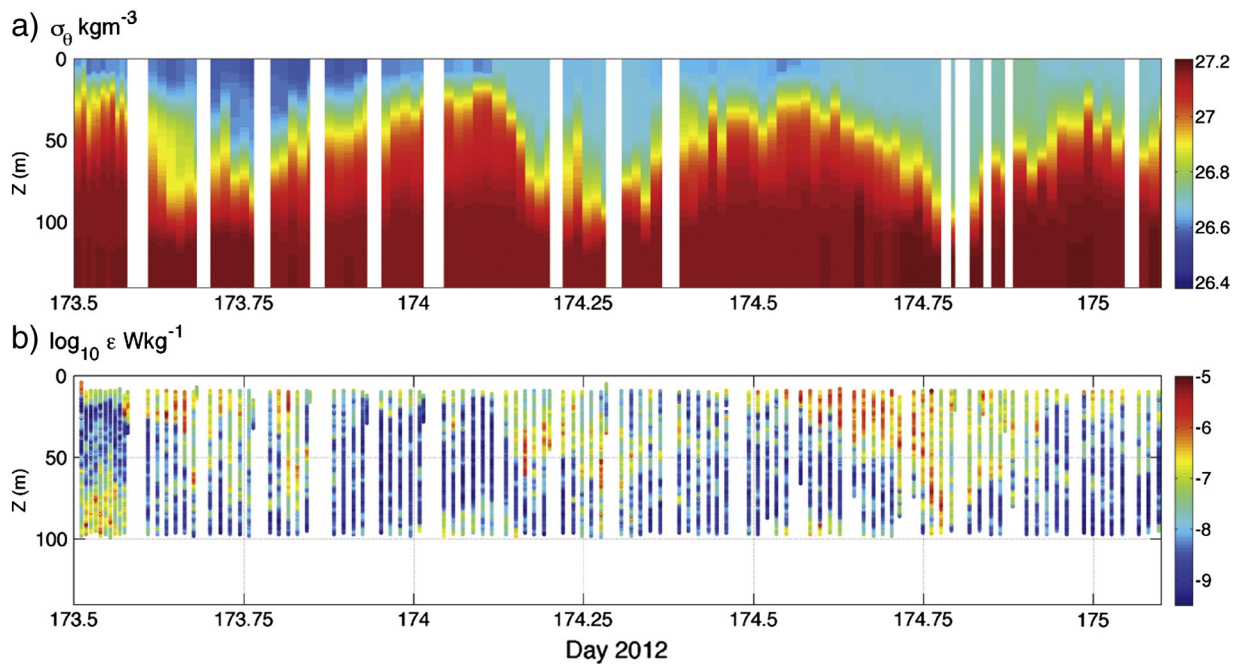


**Fig. 8.** (a) Density structure and (b)  $\log_{10}$  are shown for the most energetic period of the deployment. Three consecutive high-amplitude internal waves are characterized by high levels of turbulence in the ocean interior. Near surface turbulence appears to be drawn into the interior by vertical wave motion and pycnocline turbulence is also high and is often distinguishable from SML maxima.

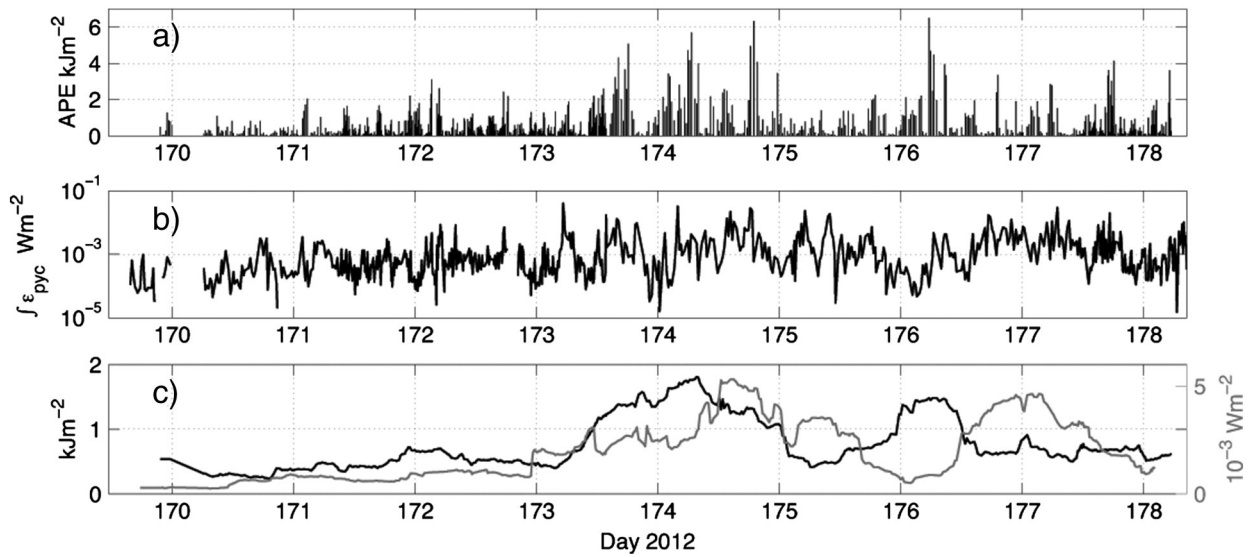


**Fig. 9.** (a) APE is highly variable however peak values are associated with the previously identified high energy period with further short-lived energetic periods from day 176.  $M_2$  averaged APE (c, black line) clearly distinguishes these periods. (b)  $\varepsilon_{pyc}$  varies over 3 orders of magnitude. Enhanced levels of turbulence after day 173 are interrupted by a well-defined minimum after day 176.  $M_2$  averaged values (c, grey line) again highlight the presence of two distinct periods of enhanced energy however there is clearly a mismatch with the timing of APE maxima.

are around  $3\text{--}4 \times 10^{-10} \text{ W kg}^{-1}$  and values are observed to range over four orders of magnitude above this.

### 3.3.1. Bottom mixed layer

Within the limited region of the BML that is resolved by the glider there is evidence of bottom boundary driven turbulence. This is identifiable as a semi-diurnal signature, particularly evident in the lower extent of the measurements around the spring tide period e.g. days 173.0, 173.5, 174.1 and 174.6. This result does not match the expected quarter-diurnal cycle of BML  $\varepsilon$  resulting from interaction between peak semidiurnal tidal energy and the seabed (Simpson et al., 1996). It appears however that this is the result of coherence between depressions in the semidiurnal internal tide and barotropic flow since bed driven turbulence is only observed during pycnocline elevations.

### 3.3.2. Surface mixed layer

Within the SML there is a high level of variability in  $\varepsilon$  which ranges over the full range of observed values. Intuitively, SML turbulence generally follows the local wind field (Fig. 6); during the first couple of days SML  $\varepsilon$  is generally low with only sporadic increases occurring over relatively small time and space scales producing a patchy distribution of turbulence. From day 172  $\varepsilon$  increases significantly and maintains a persistently high level into day 175 after which energy rapidly decreases. A second increase in wind speed on day 176 produces a further increase in SML turbulence which is often only identifiable during low frequency pycnocline depressions giving an apparent semi-diurnal periodicity to the features. This is assumed to be due to SML turbulence being constrained to a near surface layer that is often not resolved by  $\varepsilon$  measurements deeper than 10 m.

### 3.3.3. Pycnocline

Within the broad pycnocline we observe a general patchiness in  $\varepsilon$  throughout the deployment although there is a clear increase in turbulence during the already mentioned energetic periods; days 173 to 175.5 and during days 176 and 177. These periods of increased pycnocline turbulence are associated with the troughs of the internal tide. This correlation could suggest that these features are merely signatures of advection of SML turbulence. In the majority of instances however pycnocline  $\varepsilon$  maxima are distinct from the near surface signature (as is evident in Fig. 8) which is indicative of a separate or contributory internal mixing mechanism. In order to better examine

turbulence associated with internal processes we calculate the integral pycnocline dissipation rate  $\varepsilon_{pyc}$  (Fig. 9b). The pycnocline is defined here as the area between the SML and BML.  $\varepsilon_{pyc}$  is highly variable and ranges over 3 orders of magnitude. There is a clear difference in character in  $\varepsilon_{pyc}$  between the two energetic periods. During spring tides sporadic order-magnitude increases in  $\varepsilon_{pyc}$  are observed associated with high-amplitude, high-frequency internal waves. These waves may be solitons associated with the passing internal tide however the 20 minute sampling interval between consecutive upward profiles makes it difficult to confirm this. During the latter period elevated  $\varepsilon_{pyc}$  is less variable and follows a more gradual cycle centred on day 177.

Applying the same moving  $M_2$  period average to  $\varepsilon_{pyc}$  as the APE data (Fig. 9c) confirms that the majority of pycnocline turbulence is concentrated on two high energy periods, one stretching from days 173.2 to 176.0 and the another shorter period centred on day 177.0. Unlike the fairly smooth distribution of APE during the spring tide period,  $\varepsilon_{pyc}$  is highly variable. This characteristic is likely due to the more sporadic nature of turbulence and dependence of the averaged values on a few short-lived, high-energy events as is typical of pycnocline turbulence. The second period of enhanced  $\varepsilon_{pyc}$  follows a more normal distribution. Separating these periods is a clearly identifiable minimum in  $\varepsilon_{pyc}$  on day 176.04.

### 3.4. Diapycnal mixing

To assess the impact of the observed levels of turbulence on diapycnal fluxes and water column structure a pycnocline averaged turbulent mixing rate  $K_{pyc}$  is calculated using the methods of Osborn to define local turbulent diffusivity,  $K$ ,

$$K(z) = \Gamma \frac{\varepsilon(z)}{N^2(z)} \quad (8)$$

where  $\Gamma$  is a mixing efficiency assumed to be 0.2 (Osborn, 1980) and  $N^2 = -g/\rho_0 dp/dz$ .  $K_{pyc}$  (Fig. 10a) varied considerably during the measurement period, ranging over 4 orders of magnitude from  $3.7 \times 10^{-6} \text{ m}^2 \text{ s}^{-1}$  to  $2.1 \times 10^{-2} \text{ m}^2 \text{ s}^{-1}$ . The temporal and spatial average pycnocline turbulent diffusion rate (1 std) over the entire period was  $3.3 (\pm 0.1) \times 10^{-4} \text{ m}^2 \text{ s}^{-1}$ . The average pycnocline mixing rate is dominated by peak events which generally occur within the troughs of the strongest internal waves; 75% of the  $K_{pyc}$  was

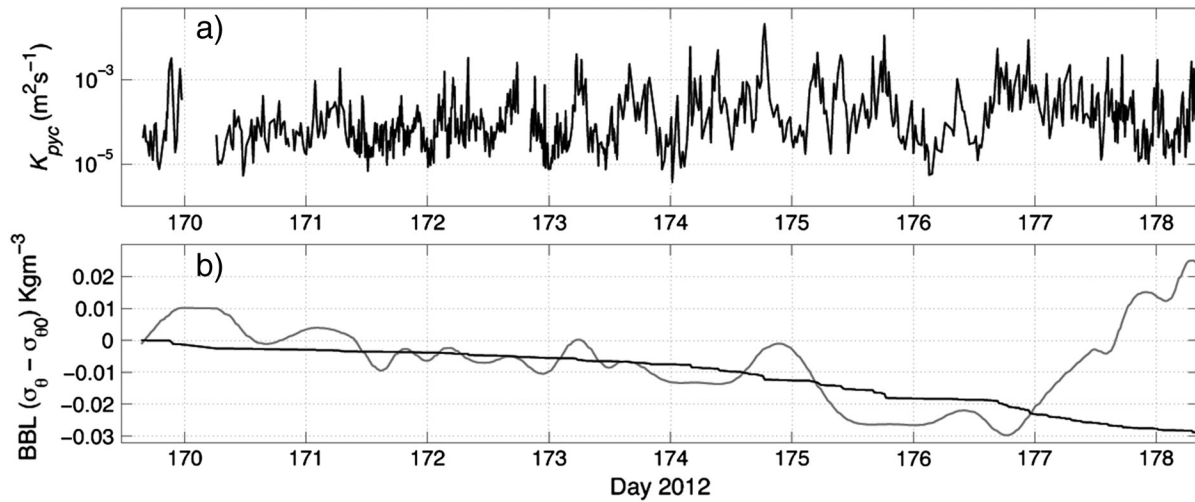


**Fig. 10.** (a) Pycnocline averaged turbulent mixing rates,  $K_{pyc}$ , vary over 4 orders of magnitude but are distinguishable into 3 distinct periods. Prior to day 172.5 values follow a low background level with short-lived sporadic increases. Following this up to a minimum on day 176.1 increases in  $K_{pyc}$  of two or three orders of magnitude are observed associated with passing high amplitude internal waves and lastly, following the minimum  $K_{pyc}$  is generally high but decreasing steadily towards the end of the deployment. (b) The predicted impact of  $K_{pyc}$  on BML density is shown alongside the observed density (offset against BML density at the start of the deployment,  $\sigma_{\theta 0}$ ).

attributable to the strongest events occurring over only 13% of the measurement period.

We now use the calculated  $K_{pyc}$  to estimate the diapycnal mass flux  $Q_{pyc}$  from,

$$Q_{pyc} = K_{pyc} \frac{\Delta\rho}{\Delta Z} \quad (9)$$

where  $\Delta\rho$  is the difference between SML and BML density and  $\Delta Z$  is the thickness of the pycnocline.  $Q_{pyc}$  therefore represents the rate of mass transport per unit square of pycnocline per second. Distributing  $Q_{pyc}$  over the calculated depth of the BML provides an estimate of the impact of the observed diapycnal flux on BML density (Fig. 10b). Our estimate of the temporal change in BML density due to diapycnal exchange is in good agreement with observations over the majority of the 9-day period. The obvious exception to this trend is the final 1.5 days of deployment when BML density is seen to increase indicating a clear shift in BML behaviour. This latter period coincides with the relatively quick cooling of the BML from day 177.0 when a steady temperature change of  $-0.21$  °C/d is observed (not shown) in contrast to a rate of  $+0.03$  °C/d prior to day 177.

### 3.5. Statistical analysis

It is clear from both raw and time averaged  $\varepsilon_{pyc}$  (Figs. 9b and 9c respectively) that turbulence is highly variable and dependent on a number of forcing mechanisms. We base this last statement on the lack of coherence with a spring-neap cycle and the observed trough in  $\varepsilon_{pyc}$  during day 176, occurring 2 days after peak spring-tide flow (according to Hopkins et al., 2014). The sporadic nature of pycnocline turbulence and broad range of values it exhibits (typically occurring over several orders of magnitude) is often not well produced in models or parameterizations of turbulence and mixing. This weakness is compounded by the relatively short time series of pycnocline turbulence and mixing that has traditionally been provided by ship-based profilers from shelf sea studies (typically equivalent to one or two tidal periods e.g. Simpson et al. (1996); Inall et al. (2000)). We therefore wish to use our extensive time series to assess the predictability of the observed characteristics of pycnocline turbulence. We consider  $\varepsilon_{pyc}$  in log space for statistical analysis (results for  $K_{pyc}$  can be considered identical). We first characterise the probability distribution of  $\varepsilon_{pyc}$  data relative to an ideal log(10)-normal distribution by comparing quantiles

in a Q-Q plot (Fig. 11, black). The majority of data conforms with the log-normal distribution with particularly good agreement within the central quantiles with some discrepancies occurring in the upper and lower extremes. To test the consistency of energy distribution over this highly variable time series we employ a histogram test (Düsterhus and Hense, 2012); data are first divided into sections by a moving window of length 55 h. This long time window was required to resolve the  $M_2$ -f frequency which was observed to be a significant component of the baroclinic kinetic energy (Hopkins et al., 2014). The difference between histograms of these data is then measured using the normalised Earth Mover's Distance (Rubner et al., 2000) which provides a measure of how alike one distribution is to the next, thus

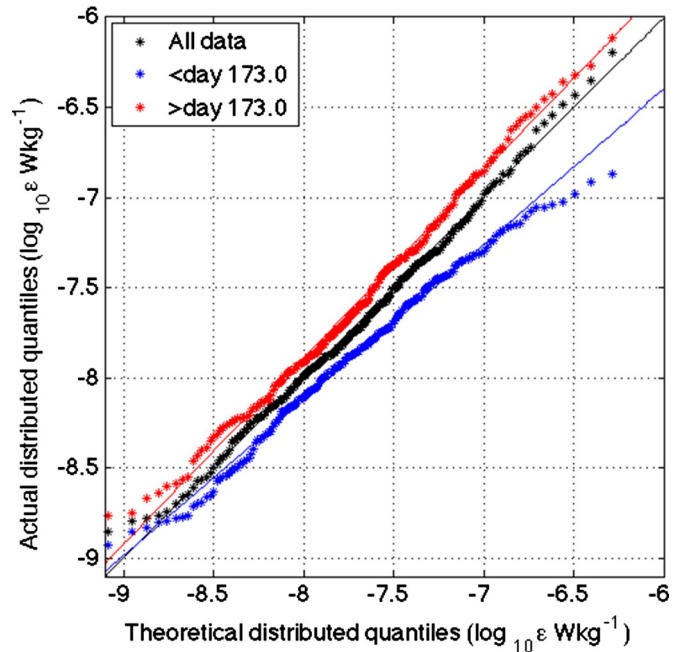


**Fig. 11.** QQ-plot of  $\log_{10}\varepsilon_{pyc}$ . Each point represents the quantiles estimated from the data, the lines show the equivalent representation of a log-normal distribution. While data from the entire period (black) is well described, we observe differing levels of agreement for data collected before (blue) and after (red) the energetic period occurring on day 173. (For interpretation of the references to colour in this figure legend, the reader is referred to the web version of this article.)

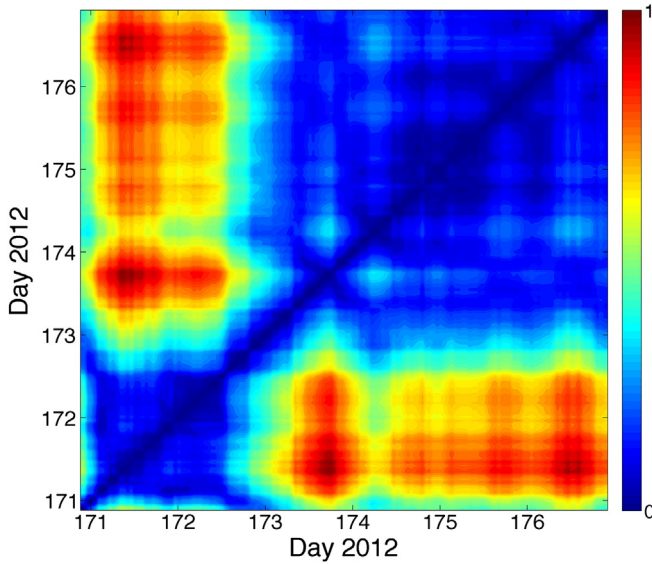


**Fig. 12.** Result from the histogram test of  $\log_{10}\epsilon_{pyc}$ . Data are divided into moving windows covering two tidal periods represented by a row and column. Each point represents the normalised difference between histograms of the two blocks represented centred on each time step. The difference is measured by the Earth Mover's Distance on histograms using 50 equally distributed quantiles between the minimum and maximum of the whole dataset.

providing a relative indicator of the energy distribution between each time period. The resulting symmetric matrix (Fig. 12) provides four distinct sections; relatively low values existing within the lower left and upper right-hand corner and relatively high values in the adjacent corners. The intersecting point for these four regions is close to day 173.0 when energy levels are seen to increase (Fig. 9c). We therefore return to Q–Q analysis separately for the periods before and after day 173.0 (Fig. 11, blue and red). The different change in mean and variance within these sections produces a change in slope however the close relation between observed and idealised distributions within the central region is maintained. An improved fit is evident in the high-energy region when considering only data after day 173. We observe a relatively poor fit in the low energy region in all plots suggesting that the noise limit of the instrument has been reached.

#### 4. Summary

- A highly energetic and variable internal wave-field is observed close to the Celtic Sea shelf break during June 2012 using data from a buoyancy controlled Slocum electric glider. Internal waves are dominated by low mode, low frequency waves close to the tidal frequency which are assumed to be the result of an internal tide generated and propagating from the nearby shelf break.
- While there is a persistent presence of a broad spectrum of internal waves, two distinct periods of enhanced baroclinic energy are identified in APE attributable to the internal tide. The first of these periods is related to a series of high energy waves associated with the spring tide period and has a peak in energy at day 174.3. The second period is clearly detached from the first and coincides with a reenergized internal tide following a short lived period of reduced internal wave activity.
- Coincident measurements of the turbulent kinetic energy dissipation rate  $\epsilon$  are used to describe the turbulence regime within the surface and bottom mixed layers (SML and BML) and pycnocline.
- While the glider does not provide full coverage of the BML signatures of semidiurnal maxima are evident. The absence of a quarter diurnal signal in these measurements is suggested to be attributable to the coherence of the barotropic and internal tides in this location; BML turbulence being advected beneath the operable region of the OMG during wave depressions.

- Turbulence in the SML appears well correlated with wind forcing. Periods of coincident high winds and high energy internal waves result in regular advection of the turbulent surface layer into the ocean interior.
- Pycnocline turbulence  $\epsilon_{pyc}$  is highly variable, ranging over 3 orders of magnitude. Similar to APE,  $\epsilon_{pyc}$  is distinguished by 2 distinct periods of enhanced energy although, as one expects from turbulent processes, is prone to greater levels of variance.
- The spring tide period results in a general increase in  $\epsilon_{pyc}$  with a peak in tidal averaged energy at day 174.6, approximately 7 h after the peak in APE. A second increase is observed centred on day 177 which relates to a period of more consistently enhanced  $\epsilon_{pyc}$ .
- Pycnocline averaged turbulent diffusion rates  $\epsilon_{pyc}$  range over 4 orders of magnitude. Time averaged  $K_{pyc}$  is  $3.3 \times 10^{-4} \text{ m}^2 \text{ s}^{-1}$ .
- Using the observed  $K_{pyc}$  and vertical density gradient the density change in the BML due to diapycnal mixing is calculated. The estimated rate of change is in good agreement with the observed reduction in BML density over the majority of the deployment period.
- Following day 177.0 a relatively rapid cooling of the BML is observed that is not readily explained.
- Statistical analysis shows how the probability distribution of pycnocline turbulence differs between high and low energy periods however  $\epsilon_{pyc}$  and  $K_{pyc}$  do maintain a near log-normal distribution over much of the energy range. Considering high and low energy periods separately improves the log-normal predictability of high energy values.

#### 5. Conclusions

The use of autonomous systems in oceanography is rapidly increasing not at least due to ready availability of buoyancy-driven ocean gliders that provide a relatively low cost, ready-to-use platform capable of long-term, high-resolution measurements with near real-time communication. In this study we use the data from our ocean microstructure glider, OMG, to provide coincident measurements of temperature, salinity and  $\epsilon$  from 10 m to 100 m depth at a site in the Celtic Sea during June 2012. We have utilised a previously developed glider flight model (MSG2010) to predict the flow past shear microstructure sensors which is required for the accurate measurement of  $\epsilon$ . A different glide angle was used during consecutively sampled downward and upward profiles to provide separable solutions to this model. Results confirm that upward and downward profiles provide estimates of  $\epsilon$  with largely identical statistical distributions over the majority of the observed range thus providing confidence in our methods. Some disparity does exist at the lower levels of detection ( $\epsilon \sim 5 \times 10^{-9} \text{ W kg}^{-1}$ ) that is accounted for by the physical asymmetry of the OMG, which results in a slightly higher noise level during upward profiles.

Our measurements identify a highly energetic internal wave-field approximately 20 km on-shelf of the Celtic Sea shelf break. While the horizontal motion of the glider results in some frequency distortion of the observed propagating wave-field, low mode, low frequency waves are clearly evident close to the semidiurnal tidal frequency. These waves are assumed to be the internal tide identified by studies at the nearby shelf break (Vlasenko et al., 2014) and further on-shelf (Hopkins et al., 2014). While the 9-day time series was insufficient to capture the full spring-neap period it is clear that the APE associated with the internal tide does not follow a typical spring-neap cycle. APE is variable but relatively low prior to day 173.2 following which energy rapidly increases, peaking during day 174 coincident with the local spring period. APE levels are not maintained however and there is an apparent interruption of high-energy waves centred on day 175.25 before APE increases for a short period during day 176 before returning to background levels.

Much of the turbulence observed using the OMG was attributable to surface forcing by the wind and this undoubtedly contributed to mixing in the upper regions of the pycnocline and helped to maintain a well

defined surface layer throughout much of the deployment. The energetic internal tide often resulted in the SML being advected deep into the ocean interior. We also observe  $\varepsilon$  maxima within the pycnocline that suggests additional internal mixing processes are present. Peaks in pycnocline turbulence are most often associated with the troughs of the internal tide. Additional input from high frequency waves is also evident which likely contributes to turbulence through additional shear and breaking. In addition to mixing by propagating internal waves we must also consider the additional shear that has often been attributed to inertial oscillations that are a common feature in the Celtic Sea and have been shown to contribute significantly to pycnocline mixing (Palmer et al., 2008; Rippeth et al., 2014). Hopkins et al. (2014) identified that inertial oscillations contributed similar levels of kinetic energy as the internal tide at two nearby sites during the OMG deployment.

Pycnocline turbulence follows a similar pattern to APE; a relatively quiescent period prior to day 173.0 is followed by rapidly increasing  $\varepsilon_{pyc}$  peaking during day 174. This peak energy period is followed by a distinct trough at day 176.0 before a shorter period increase in  $\varepsilon_{pyc}$  centred on day 177.0. While  $\varepsilon_{pyc}$  is more variable than APE, as one might expect from the sporadic nature of turbulence, there is a clear match in behaviour with an apparently persistent delay in peaks and troughs of the majority of features. This delay suggests that while the increase in APE promotes pycnocline turbulence and mixing it is not the only contributing mechanism.

Hopkins et al. (2014) suggest that during the deployment period, variable wind forcing at the shelf break acted to reduce local stratification that in turn produced a change in slope criticality that modified the amount of baroclinic energy that is able to propagate on-shelf. The variability in APE and subsequently  $\varepsilon_{pyc}$  might be explained by such a change in structure at the generation zone for the observed internal waves. Using a sensible estimate of the first mode internal wave speed ( $\sim 0.4 \text{ ms}^{-1}$ ) one would expect the impact of changes in shelf break forcing should therefore be observed by the OMG within approximately 14 h.

From the combined density and  $\varepsilon$  data we suggest that pycnocline turbulence and mixing at this location are controlled by a combination of both internal waves (via breaking and enhanced shear) and inertial oscillations (which further contribute to pycnocline shear) with additional input from boundary processes. We suggest that strong winds during the spring period (Fig. 6) may have acted to dampen the generation of internal waves for two tidal periods and pycnocline mixing was subsequently also reduced. The severe gales that were experienced prior to the OMG deployment may also have played a role in the reduced energy period prior to day 171.5. The delay in behaviour of  $\varepsilon_{pyc}$  relative to APE is not readily explained however it does suggest that there is memory in the system which may be dependent on additional controls on pycnocline stability such as inertial shear.

The calculated density flux attributable to the observed levels of pycnocline mixing accounts for much of the observed decrease in BML density as warmer, fresher surface water is mixed through the pycnocline. This suggests that vertical mixing is the dominant control on modification of the BML. Since our observations were made close to the shelf break this result has important implications for ocean-shelf exchange; implying that exchange at the nearby shelf break is not the result of long-term horizontally diffusive processes. This suggests that exchange is generally weak and likely dependent on large-scale events such as on-shelf intrusion of the slope current (Huthnance, 1995). The observed efficiency of the shelf break generated internal wave-field in promoting mixing of fresh surface water and dense bottom water will likely act to suppress across-shelf exchange by entraining surface water into the bottom layer and vice versa to maintain a reduced horizontal gradient at the near shelf break region. These results have further important implications for predicted climate change scenarios; modification of the seasonal stratification cycle by rising temperatures and increased intensity and occurrence of storms will modify the

generation and propagation of internal waves and so likely impact on critical exchange mechanisms at the shelf break region.

Pycnocline turbulence and mixing is notoriously difficult to predict and extensive research efforts are focused on providing improved understanding and parameterization of ocean mixing. We have shown that shorter time-series than those analysed here are unlikely to provide a suitably estimate of  $\varepsilon_{pyc}$  and  $K_{pyc}$  due to high levels of variability and changing probability distributions during high and low-energy periods. Although much of the variability is explained by a log-normal distribution we observe high energy values to deviate from the behaviour of other values when the whole dataset is considered. An increased correlation is achieved however when data are separated into low and high energy periods, in this case prior to and following day 173.0. This result gives some confidence to those modelling pycnocline turbulence since it suggests that a  $\varepsilon_{pyc}$  and  $K_{pyc}$  produce a predictable (i.e. log-normal) distribution about the mean value. While the difficult task of predicting the mean remains this understanding could help improve the temporal and spatial distributions of pycnocline turbulence, which is often lacking from region-scale models.

## Acknowledgements

The authors gratefully acknowledge the support of the NERC which provided funding for the FASTNet programme under grant NE/I030259/1 and an Advanced Fellowship NE/F014821/1 for JAMG. This work could not have occurred without the expert assistance of the officers and crew of the RRS Discovery (cruise D376 led by Capt. Antonio Gatti), the NOC Marine Autonomous and Robotic Systems facility (MARS), Dave Jones at the NOC and staff at Teledyne Webb Research.

## References

- Baines, P.G., 1982. On internal tide generation models. *Deep Sea Res.* A 29, 307338.
- Boyd, T., Inall, M., Dumont, E., Griffiths, C., 2010. AUV observations of mixing in the tidal outflow from a Scottish sea loch. *Autonomous Underwater Vehicles (AUV)*, 2010 IEEE/OES, pp. 1–9.
- Düsterhus, A., Hense, A., 2012. Advanced information criterion for environmental data quality assurance. *Adv. Sci. Res.* 8, 99–104.
- Fer, I., Peterson, A.K., Ullgren, J.E., 2014. Microstructure measurements from an underwater glider in the turbulent Faroe Bank Channel overflow. *J. Atmos. Ocean. Technol.* 31, 1128–1150.
- Goodman, L., Levine, E.R., Lueck, R.G., 2006. On measuring the terms of the turbulent kinetic energy budget from an AUV. *J. Atmos. Ocean. Technol.* 23(7).
- Green, J.A.M., Simpson, J.H., Legg, S., Palmer, M., 2008. Internal waves, baroclinic energy fluxes and mixing at the European shelf edge. *Cont. Shelf Res.* 28 (7), 937–950. <http://dx.doi.org/10.1016/j.csr.2008.01.014>.
- Holt, J., Butenschon, M., Wakelin, S.L., Artioli, Y., Allen, J.L., 2012. Oceanic controls on the primary production of the northwest European continental shelf: model experiments under recent past conditions and a potential future scenario. *Biogeosciences* 9, 97–117.
- Hopkins, J.E., Stephenson, G.R., Green, J.A.M., Inall, M.E., Palmer, M.R., 2014. Storms modify baroclinic energy fluxes in a seasonally stratified shelf sea: inertial-tidal interaction. *J. Geophys. Res.* 119. <http://dx.doi.org/10.1002/2014JC010011>.
- Huthnance, J.M., 1995. Circulation, exchange and water masses at the ocean margin: the role of physical processes at the shelf edge. *Prog. Oceanogr.* 35 (4), 353–431.
- Inall, M.E., Rippeth, T.P., Sherwin, T.J., 2000. Impact of nonlinear waves on the dissipation of internal tidal energy at a shelf break. *J. Geophys. Res.* 105 (C4), 86878705.
- Inall, M., Aleynik, D., Boyd, T., Palmer, M., Sharples, J., 2011. Internal tide coherence and decay over a wide shelf sea. *Geophys. Res. Lett.* 38 (23).
- Johnston, T.M.S., Rudnick, D.L., Carter, G.S., Todd, R.E., Cole, S.T., 2011. Internal tidal beams and mixing near Monterey Bay. *J. Geophys. Res.* 116. <http://dx.doi.org/10.1029/2010JC006592> C03017.
- Jones, C., Creed, E., Glenn, S., Kerfoot, J., Kohut, J., Mudgal, C., Schofield, O., 2005. Slocum gliders: a component of operational oceanography. *Proc. 14th Int. Symp. on Unmanned Untethered Submersible Technology*.
- Kang, D., Fringer, O., 2010. On the calculation of available potential energy in internal wave fields. *J. Phys. Oceanogr.* 40 (11).
- Kundu, P.K., 1990. *Fluid Mechanics*. Academic Press, Inc., p. 638.
- Lamb, K.G., 2007. Energy and pseudoenergy flux in the internal wave field generated by tidal flow over topography. *Cont. Shelf Res.* 27 (9), 1208–1232.
- Lueck, R.G., Picklo, J.J., 1990. Thermal inertia of conductivity cells: observations with a sea-bird cell. *J. Atmos. Ocean. Technol.* 7, 756768.
- MacKinnon, J.A., Gregg, M.C., 2003. Mixing on the late-summer New England shelf solibores, shear, and stratification. *J. Phys. Oceanogr.* 33, 14761492.

- Macoun, P., Lueck, R., 2004. Modeling the spatial response of the airfoil shear probe using different sized probes. *J. Atmos. Ocean. Technol.* 21 (2).
- Merckelbach, L., Smeed, D., Griffiths, G., 2010. Vertical water velocities from underwater gliders. *J. Atmos. Ocean. Technol.* 27 (3), 547–563.
- Moum, J.N., Caldwell, D.R., Paulson, C.A., 1989. Mixing in the equatorial surface layer and thermocline. *J. Geophys. Res.* 94 (C2), 20052022.
- Moum, J.N., Farmer, D.M., Smyth, W.D., Armi, L., Vagle, S., 2003. Structure and generation of turbulence at interfaces strained by internal solitary waves propagating shoreward over the continental shelf. *J. Phys. Oceanogr.* 33, 20932112.
- Moum, J.N., Klymak, J.M., Nash, J.D., Perlin, A., Smyth, W.D., 2007. Energy transport by nonlinear internal waves. *J. Phys. Oceanogr.* 37 (7), 1968–1988.
- Moum, J.N., Nash, J.D., Klymak, J.M., 2008. Small-scale processes in the coastal ocean. *Oceanography* 21 (4), 22–33.
- Nash, J.D., Shroyer, E.L., Kelly, S.M., Inall, M.E., Duda, T.F., Levine, M.D., Jones, N.L., Musgrave, R.C., 2012. Are any coastal internal tides predictable? *Oceanography* 25 (2), 8095.
- Nasmyth, P.W., 1970. *Oceanic Turbulence*. (PhD thesis) University of British Columbia.
- Oakey, N.S., 1982. Determination of the rate of dissipation of turbulent energy from simultaneous temperature and velocity shear microstructure measurements. *J. Phys. Oceanogr.* 12 (3), 256–271.
- Osborn, T.R., 1980. Estimates of the local rate of vertical diffusion from dissipation measurements. *J. Phys. Oceanogr.* 10 (1), 83–89.
- Palmer, M.R., Rippeth, T.P., Simpson, J.H., 2008. An investigation of internal mixing in a seasonally stratified shelf sea. *J. Geophys. Res.* 113. <http://dx.doi.org/10.1029/2007JC004531> (C12005).
- Palmer, M.R., Inall, M.E., Sharples, J., 2013. The physical oceanography of Jones bank: a mixing hotspot in the Celtic Sea. *Prog. Oceanogr.* 117, 924.
- Pingree, R.D., Mardell, G.T., Cartwright, D.E., 1981. Slope turbulence, internal waves and phytoplankton growth at the Celtic Sea shelf-break [and discussion]. *Philosophical transactions of the royal society of London. J. Math. Phys. Sci. Ser. A* 302 (1472), 663–682.
- Rippeth, T.P., Lincoln, B.J., Kennedy, H.A., Palmer, M.R., Sharples, J., Williams, C., 2014. Impact of vertical mixing on sea surface pCO<sub>2</sub> in temperate seasonally stratified shelf seas. *J. Geophys. Res. Oceans* 06 (2014). <http://dx.doi.org/10.1002/2014JC010089> ((online)).
- Rubner, Y., Tomasi, C., Guibas, L.J., 2000. The earth movers distance as a metric for image retrieval. *Int. J. Comput. Vis.* 40 (2), 99–121.
- Sandstrom, H., Oakey, N.S., 1995. Dissipation in internal tides and solitary waves. *J. Phys. Oceanogr.* 25, 604614.
- Scotti, A., Beardsley, R., Butman, B., 2006. On the interpretation of energy and energy fluxes of nonlinear internal waves: an example from Massachusetts Bay. *J. Fluid Mech.* 561, 103–112.
- Sharples, J., Tweddle, J.F., Green, J.A.M., Palmer, M.R., Kim, Y.-N., Hickman, A.E., Holligan, P.M., Moore, C.M., Rippeth, T.P., Simpson, J.H., Krivtsov, V., 2007. Spring-neap modulation of internal tide mixing and vertical nitrate fluxes at a shelf edge in summer. *Limnol. Oceanogr.* 52 (5), 1735–1747.
- Shroyer, E.L., Moum, J.N., Nash, J.D., 2010. Energy transformations and dissipation of nonlinear internal waves over New Jersey's continental shelf. *Nonlinear Process. Geophys.* 17 (4), 345–360.
- Simpson, J.H., Crawford, W.R., Rippeth, T.P., Campbell, A.R., Cheok, J.V., 1996. The vertical structure of turbulent dissipation in shelf seas. *J. Phys. Oceanogr.* 26 (8), 1579–1590.
- St Laurent, L.C., Thurnherr, A.M., 2007. Intense mixing of lower thermocline water on the crest of the Mid-Atlantic ridge. *Nature* 448 (7154), 680–683.
- Thomas, H., Bozec, Y., Elkalay, K., De Baar, H.J., 2004. Enhanced open ocean storage of CO<sub>2</sub> from shelf sea pumping. *Science* 304 (5673), 1005–1008.
- Vlasenko, V., Stashchuk, N., Inall, M.E., Hopkins, J.E., 2014. Tidal energy conversion in a global hot spot: On the 3D dynamics of baroclinic tides at the Celtic Sea shelf break. *J. Geophys. Res. Oceans* 119, 32493265.
- Wolk, F., Yamazaki, H., Seuront, L., Lueck, R.G., 2002. A new free-fall profiler for measuring biophysical microstructure. *J. Atmos. Ocean. Technol.* 19 (5), 780–793.
- Wolk, F., Lueck, R.G., St Laurent, L.C., 2009. Turbulence measurements from a glider. *OCEANS 2009, MTS/IEEE Biloxi – Marine Technology for Our Future: Global & Local Challenges*, p. 16.